Li-Na Wu*, Shao-Yi Wu, Fei-Hu Liu and Qing Zhang

Studies of the Electronic, Optical, and Thermodynamic Properties for Metal-Doped LiH Crystals by First Principle Calculations

https://doi.org/10.1515/zna-2020-0057 Received February 23, 2020; accepted February 25, 2020

Abstract: Hydrogen as a clean and abundant energy source with high energy density is considered as a promising solution to future energy crisis, although storage of hydrogen is still challenging. Lithium hydride can be an alternative for hydrogen storage because of its small volume and high storage capacities, although this material is unsuitable as hydrogen reservoir because of its high dehydriding temperature. The density functional theory calculations based on the first principle are applied to study the physical properties of LiH without and with different metal M (M=Al, Fe, and Ru). The M-substituted systems exhibit lower dehydriding temperatures than the pure LiH, and Li_{1-x}Al_xH may be the most suitable candidate for hydrogen reservoir owing to the high hydrogen content and low dehydriding temperature. The stability and thermodynamic properties for hydrogen storage are discussed for these systems. The kinetics and the optical activity in the visible and infrared regions are enhanced by the metal dopants, characterized by the M impurity bands in the band gaps of the doped systems.

Keywords: Electronic Structures; Formation Energy; Hydrogen Storage; Lithium Hydride; Optical Properties.

1 Introduction

Hydrogen is an ideal energy carrier for various applications. One of the key challenges is the storage of hydrogen with high storability and portability. Owing to their high

Xi'an Technological University, Xi'an 710021, China, E-mail: wulina@xatu.edu.cn

Shao-Yi Wu and Qing Zhang: School of Physics, University of Electronic Science and Technology of China, Chengdu 610054, China, E-mail: shaoyi_wu@163.com (S-Y. Wu); zq464036287@163.com (Q. Zhang)

*Corresponding author: Li-Na Wu, School of Science,

Fei-Hu Liu: School of Science, Xi'an University of Posts and Telecommunications, Xi'an 710021, China, E-mail: liufeihu@xupt.edu.cn

density [1], reversibility [2], and safety [3], metal hydrides (MHs) are more promising candidates for hydrogen storage than other media. MHs are especially suitable for stationary on-site solid-state hydrogen storage because of their relatively low operating pressures and temperatures [4]. Intensive research has been carried out on MHs recently for the improvement of hydrogenation properties [1]. For example, alanates and magnesium hydride are remarkable hydrogen storage materials because of their high storage capacities [5–8]. However, the primary and the most important process of hydrogen storage is hydrogen absorption with high content in materials. As the simplest MH, LiH is applicable for hydrogen storage [9-11] because of its largest hydrogen content [12, 13] and its high efficiency in nuclear industry [14]. However, it has too high reaction heat to be used for fuel cell vehicles. Fortunately, MHs can be destabilized by doping with other metal elements and their oxides [15–18] or alloying with other elements [19-21]. For instance, as one of the best candidates for hydrogen storage, LiAlH4 can release 7.9 wt.% H below 220 °C [22]. Through reactive ball milling [23], addition of Fe to MgH₂ can effectively improve the hydrogen sorption kinetic properties of the system [24]. Ruthenium plays a key role in Ru-catalysts for formic acid dehydrogenation in recyclable systems [25]. Remarkably, transition metal (TM) dopants in materials may usually enhance the optical absorption in the infrared and visible regions [26] by introducing a metal-induced gap band (MIGB) between the valence band (VB) and the conduction band (CB) [27, 28]. In general, the ideal hydrogen storage materials require favorable thermodynamic properties with sufficiently rapid kinetics of hydrogen charging/discharging, and attempts should be made to enhance the reversibility of the hydriding/dehydriding reactions. However, studies for this simplest MH, LiH, are relatively scarce up to now. Thus, further investigations are worthy to be carried out on the electronic and thermodynamic properties of LiH and suitable enhancement of the hydrogen storage properties with metal dopants.

In this paper, the structural, electronic, thermodynamic, and optical properties and hydrogen storage of LiH without and with various metal M (M=Al, Fe, and Ru) dopants are studied from the density functional theory

(DFT) calculations based on the quantum chemistry and solid state physics software package CP2K (version 4.1) by Universität Zürich (Zürich, Switzerland) and Universität Paderborn (Paderborn, Germany) [29] and Cambridge sequential total energy package (CASTEP) [30], which have been widely applied in previous works [31–34].

This paper is organized as follows: The computational methods are illustrated in Section 2. In Section 3, the information about the optimized structures and properties (e.g. electronic structures and thermodynamic and optical properties) of LiH and Li_{1-x}M_xH are discussed and compared. Finally, the conclusions are summarized in Section 4.

2 Method of Calculation

To obtain the stable structures for the substitutional metals M (M=Al, Fe, and Ru) on the Li site in the LiH crystal, geometry optimizations (GEO-OPT) are employed with CP2K/Quickstep [35] by using the mixed Gaussian and plane wave approaches, GPW and GAPW [36, 37]. The periodic calculations with periodic boundary conditions are performed. The simulation cell containing 64 atoms (Li₃₁MH₃₂) is tested, with the periodic boundary conditions imposed along X (// [100]), Y (// [010]) and Z (// [001]) axes. The convergence tests of the total energy with respect to the plane-wave energy cutoff have been carefully examined. The final set of energies and geometry optimization is computed with an auxiliary plane wave grid cutoff of 500 Ry, without any other constraints except the symmetries. All geometry optimizations and thermodynamic property calculations are based on generalised gradient approximation (GGA) functional PBE [38], double-ζ Gaussian basis set [39] in combination with Goedecker-Teter-Hutter pseudopotentials [40].

The hybrid functional PBEO (25 % of Fock-exchange) [41] in CASTEP code is adopted to study the electronic structures and optical properties, which are determined by using the norm-conserving pseudopotentials [42]. Brillouin zone sampling is performed with a $2 \times 2 \times 2$ k-point grid. The high symmetric points are chosen as W(0.50, 0.25, 0.75), L(0.50, 0.50, 0.50), G(0.00, 0.00, 0.00), X(0.50, 0.00, 0.50), and K(0.375, 0.375, 0.75), as well as Z(0.00, 0.00, 0.50), M(0.50, 0.50, 0.00), R(0.00, 0.50, 0.50), A(0.50, 0.00, 0.00), and Y(0.00, 0.50, 0.00).

Non-spin-polarization is performed in all calculations for LiH and Li_{1-x}Al_xH systems, whereas spin-polarized calculations are made for Li_{1-x}Fe_xH and Li_{1-x}Ru_xH systems because of paramagnetism. The number of unpaired electron in two d^7 systems is 3 or 1, with the spin S = 3/2 or 1/2 for Fe⁺ or Ru⁺, respectively.

3 Results and Discussions

3.1 Structural Properties

LiH is crystallized in the NaCl-type structure (FM-3M, space group no. 225). All the calculations are carried out using a $2 \times 2 \times 2$ super-cell containing 31 Li atoms, 1 metal M

atom, and 32 H atoms, denoted henceforth as Li₃₁MH₃₂. The metal (M=Al, Fe, and Ru) doped concentration is x = 3.125 %. The lattice constants of Li. Al. Fe. and Ru are shown in Table 1, which are comparable with the experimental data [45]. Here, because of difference of cells after doping, the lattice parameters a of the supercell we used are twice the lattice constants a_0 of pure LiH, i.e. $a = 2a_0$.

As a relaxed parameter, the lattice parameters for LiH with and without M dopants are optimized by fixing the relative atomic position and varying the lattice parameter a by ± 10 % of the experimental data $2a_0$. The total energy of LiH, as a function of volume, before and after being doped with a certain element (Al, Fe, and Ru), is calculated using the PBE functional and double- ζ basis set with Goedecker-Teter-Hutter pseudopotentials. The results are shown in Figure 1. The structural parameters, the bulk modulus B_0 , and its first derivative B'_0 with respect to the pressure listed in Table 2 are given by fitting the total energies to the Murnaghan equation of state [46]:

$$E(V) = E_0 + \frac{9V_0B_0}{16} \left\{ \left[\left(\frac{V_0}{V} \right)^{2/3} - 1 \right]^3 B_0' + \left[\left(\frac{V_0}{V} \right)^{2/3} - 1 \right]^2 \left[6 - 4 \left(\frac{V_0}{V} \right)^{2/3} \right] \right\}$$
(1)

where E_0 is the minimum energy and V_0 is the equilibrium volume. The simulated a_0 (\approx 4.024 Å) and B_0 (\approx 33.59 GPa) of LiH are close to the experimental values ($a_0 \approx 4.083 \text{ Å}$ [47] and $B_0 \approx 33.60$ GPa [48]).

After the metal M doping, the local structures of [MH₆] octahedra are also modified with respect to the host LiH. The distances between the nearest neighbor (nn) H atoms and the central metal M are illustrated in Table 3. The increase of the cation-anion distance in the $[AlH_6]^{5-}$ center related to the host $[LiH_6]^{5-}$ octahedron is attributable to the larger ionic radius (≈0.93 Å [49]) of impurity Al⁺ than host Li⁺ (≈0.76 Å [47]). For Fe replacing a host Li in LiH crystal, the symmetry of the [FeH₆]⁵⁻ cluster maintains cubic with the threefold orbitally degenerated ground state ${}^{4}T_{1g}$ of high spin (S=3/2) under intermediate crystal fields. The slightly smaller Fe-H bond

Table 1: Lattice parameters of the simple elements.

Element	Space group	Crystalline structure	lonic radius (+1)	a/Å	c/Å
Li	229-lm3m	bcc	0.76 [43]	3.5092	3.5092
Al	225-Fm3m	fcc	0.93 [44]	4.0495	4.0495
Fe	227-lm3m	bcc	_	2.8664	2.8664
Ru	194-P6 ₃ /mmc	hcp	-	2.7058	4.2816

DE GRUYTER

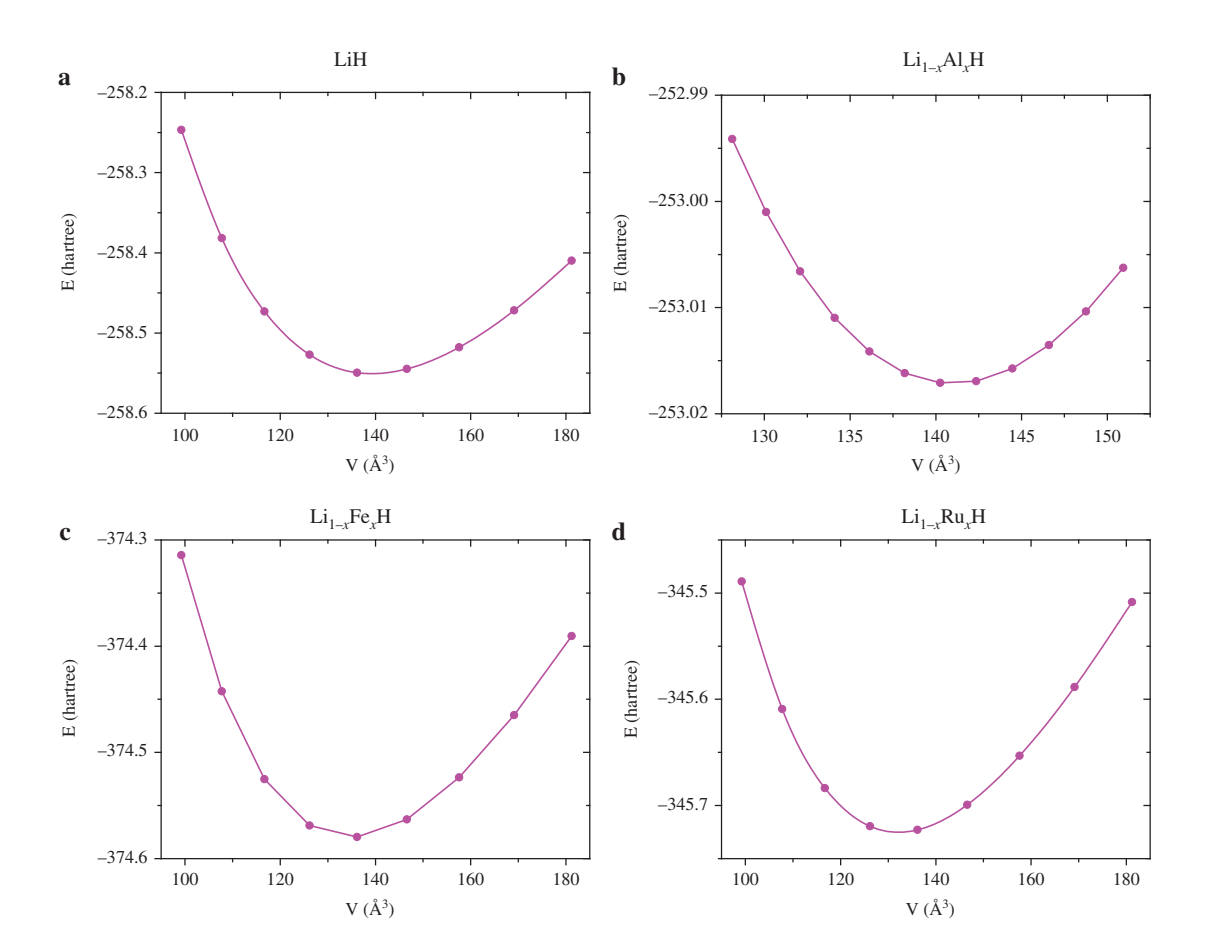


Figure 1: Calculated free energy versus supercell volume for pure LiH and $Li_{1-x}M_xH$. (a) LiH, (b) $Li_{1-x}Al_xH$, (c) $Li_{1-x}Fe_xH$, and (d) $Li_{1-x}Ru_xH$.

 $\textbf{Table 2:} \ \, \textbf{Optimized structural parameters and the thermodynamical quantities of pure LiH and Li_{31}MH_{32} \ (M=Al, Fe, and Ru).}$

Systems	Relaxed parameters a(Å)		Cg (wt.%)	B ₀ (GPa)	B′ ₀	ΔH (kJ/mol H)
		Н	M			
Li ₃₂ H ₃₂	8.24766	12.681	_	33.59	3.35	-94.06
Li ₃₁ AlH ₃₂	8.26399	11.755	9.832	42.03	3.52	-73.14
Li ₃₁ FeH ₃₂	8.14150	10.636	18.416	40.07	3.49	-79.76
Li ₃₁ RuH ₃₂	8.08434	9.255	29.008	41.68	3.48	-84.92

Table 3: Local structure of $[MH_6]^{5-}$, the distance between nn H and central metal M (Al, Fe, and Ru), the spin and Mulliken charge of the metal M, and the overlap population (OP) of the bond H–M.

Systems	Spin ($\hbar/2$)	Charge (e)	OP (e)	X (Å)	Y (Å)	Z (Å)	R (Å)
Li ₃₁ AlH ₃₂	0	-0.57	0.04	2.2546	2.2546	2.2546	2.2546
Li ₃₁ FeH ₃₂	2.85	-0.96	0.59	1.8329	1.8329	1.8329	1.8329
Li ₃₁ RuH ₃₂	0.79	-1.46	0.88	1.8169	1.8169	1.9430	1.8589

length than Li–H in host LiH may be largely ascribed to the strong covalency and hence remarkable Fe–H orbital hybridization. As for the $[{\rm RuH_6}]^{5-}$ cluster, the distances between central ${\rm Ru^+}$ and nn H $^-$ exhibit similar uniform shrinkage by about 9.8 % and extra tetragonal elongation due to the Jahn–Teller effect, characterized by the

axial elongation $a \approx 0.016$ Å, with the error less than 1 % due to the limits of the DFT calculations. Then the original cubic two-fold orbitally degenerated 2E_g ground state is split into two orbital singlets $^2A_{1g}$ and $^2B_{1g}$, with the former lying lowest. Similar tetragonally elongated d^7 centers with low spin (S=1/2) were also investigated

with high order perturbation formulas [50] and DFT calculations [43, 51, 52]. In fact, substitution of Li⁺ by obviously covalent Fe⁺ or Ru⁺ may induce the enhancement of metal-ligand covalent interactions and hence shorter average bond lengths. The calculated spins in Table 3 for Feand Ru-doped LiH suitably support the high (S = 3/2) and low (S = 1/2) spins of the related systems, respectively, and can be regarded as valid in physics.

3.2 Band Structures and Density of States

The electronic structures can offer important information about the electronic and optical characteristics of materials. The density of states (DOS) is used to analyze and explain the effect of the metal dopants on the stability and kinetics of the hydrogen absorption-desorption in $Li_{1-x}M_xH$. For this purpose, the band structures and (total and projected) DOS of LiH with and without M dopants are calculated and shown in Figures 2 and 3. The Fermi level presented with a gray line is set as zero of energy. It is well known that the DFT calculations based on localdensity approximations and GGA approximations underestimate the bandgaps [44, 53], while meta-GGAs and hybrid functionals are more accurate and reliable [54]. So, the PBEO functional is adopted in the present calculations for bandgaps, which yields consistent results with the experimental data.

3.2.1 Pure LiH

The electronic structures of pure LiH exhibit a nonmetallic character with the energy gap of 4.157 eV (Figs. 2a and 3a) at X point, which is slightly lower than the experimental value 4.94 eV [55]. The above discrepancy between theory and experiment may be ascribed to the DFT calculations, which usually suffer from the errors in the estimation of the bandgap [56] and yield a larger band width and smaller gap. The Fermi level locates at the top of the VB. The whole VB originates mainly from H-s orbital. The first part of VB (so called "high VB") from -0.87 eV to the Fermi level arises almost from the H-s state. The second part of VB (so called "low VB") from -5.7 to -0.87 eV consists mainly of the H-s state slightly hybridized with the Li-s state. The CB is almost attributed to Li-s state. The barely hybridized states reveal the ionicity of LiH.

3.2.2 LiH Doped with Metals

In the unit cell of pure LiH, H and Li atoms locate at equivalent sites and exhibit similar DOS. However, the symmetry is disturbed when the Li atom at (0.5, 0.5, 0.5) position in the 4 \times 4 \times 4 supercell is substituted by an M dopant. Thus, more Li and H atoms become inequivalent and lead to the significantly different DOS. In the following discussion, the PDOS of only two kinds of inequivalent H or Li atoms is considered: six nn ligands H (labeled as H1), next nearest neighbor (nnn) Li (labeled as Li1), and farther H or Li (labeled as H2 or Li2) atoms away from the impurity. The DOS of farther H and Li atoms in the doped systems are almost the same as those in pure LiH.

To clarify the effect of the doped elements (M=Al, Fe, and Ru) on the electronic structures of LiH, the band structures and DOS of $Li_{1-x}M_xH$ are plotted in Figures 2 and 3, respectively. The doped systems exhibit the more dispersive DOS and the wider bands. Moreover, the M dopants induce a MIGB between VB and CB [27, 28] and may improve the utilization of visible and infrared light. This point is to be discussed in the following subsection. The electronic structures of $Li_{1-x}M_xH$ show similar VB and CB patterns to pure LiH, except the MIGB in the middle of the band gap arising from the d-orbitals of Fe and Ru or s- orbitals of Al where the contribution to the total DOS comes mainly from the impurities M.

Comparing with pure LiH, another remarkable feature of the energy band for M-substituted LiH is that the Fermi level shifts up towards the CB. The strong hybridization of Fe (or Ru) -d or Al-p with H-s orbitals in the doped systems is dissimilar to the weak hybridization between the nn H and Li in pure LiH. Naturally, no hybridization is found between M and Li atoms, indicating no binary LiM after releasing hydrogen. This point is in agreement with the results of Section 3.5, where addition of metal M in LiH leads to the decreases of stability and desorption temperature of the systems. It is noted that LiH doped with Al exhibits the highest DOS near the Fermi level.

From Figure 3c,d, the fivefold degenerated *d* orbitals are divided into an orbital triplet t_{2g} and an orbital doublet e_g , with the former lying lower [57]. Similar d level splittings due to the crystal fields were also reported with DFT calculations [43, 51, 52]. The positions of the two TM impurity levels (t_{2g} and e_g) shift towards the CB, and consequently, the distance between e_{2g} and the CB decreases, especially for M=Ru. This point is also consistent with the calculations of formation heat, which shows similar decreasing trend from Ru to Fe.

3.3 Electronic Spin Configuration

According to the crystal field theory [58], Fe⁺ and Ru⁺ ions with the same d^7 configurations can exhibit dissimilar behaviors in octahedral crystal fields, dependent

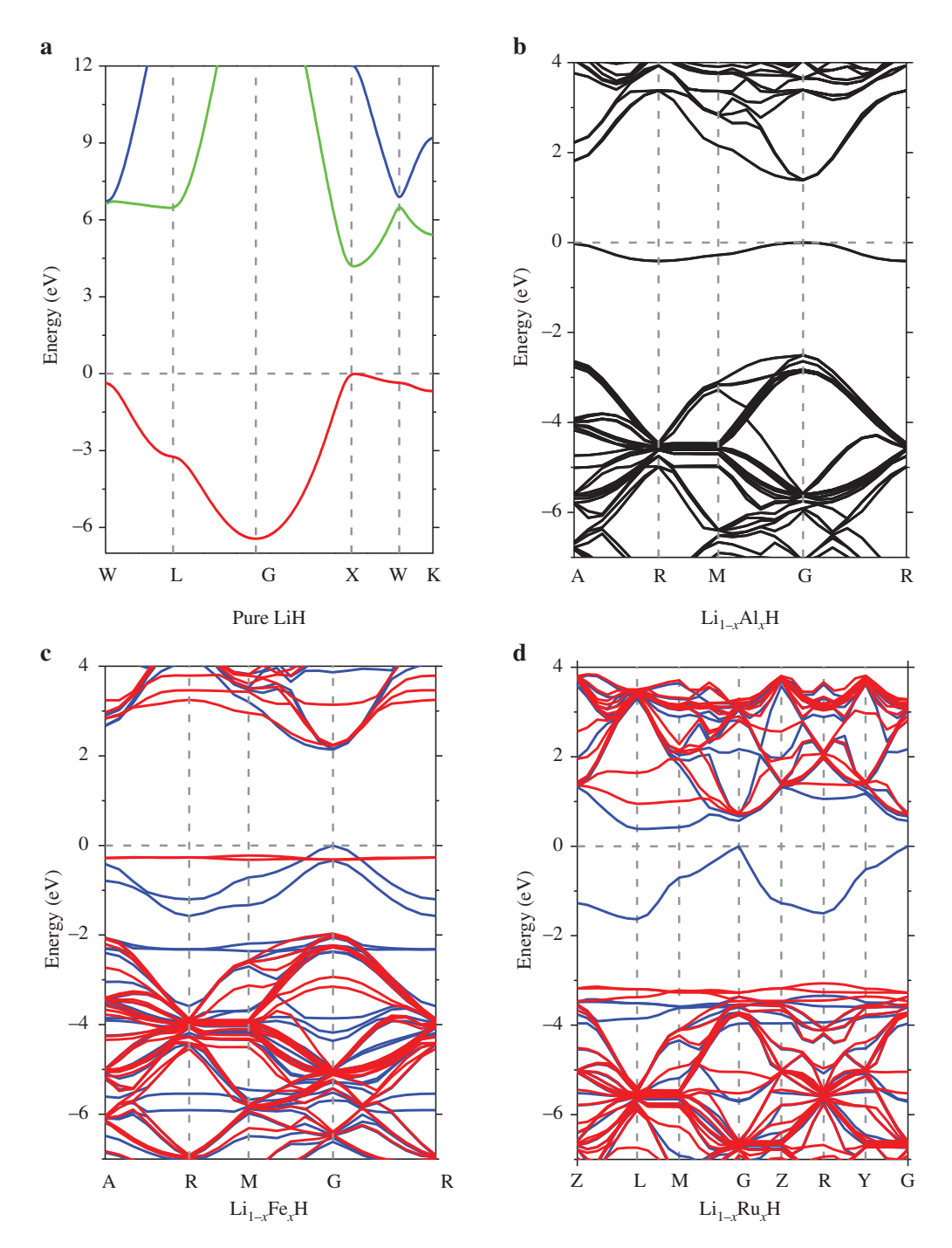


Figure 2: Band structures of LiH without and with the dopants. A MIGB occurs between the VB and CB for $Li_{1-x}M_xH$ system. In the band structure of the spin-polarized $Li_{1-x}Fe_xH$ (c) and $Li_{1-x}Ru_xH$ (d), blue and red lines represent the spin-up and spin-down states, respectively. (a) Pure LiH, (b) $Li_{1-x}Al_xH$, (c) $Li_{1-x}Fe_xH$, and (d) $Li_{1-x}Ru_xH$.

on the competition between the crystal field stabilization energy (Δ) and intra-orbital electron pairing energy (Π) (see Fig. 4). For Fe⁺ with $\Delta < \Pi$, the two 3d electrons are more likely to occupy the higher e_g orbitals than to pair with the electrons in the lower t_{2g} orbitals, associated with the case of weak field with high spin (i.e. $t_{2g}{}^5e_g{}^2$ configuration with S=3/2). For Ru⁺ with $\Delta > \Pi$, the stronger

crystal field forces the six 4d electrons to pair with each other in the lower t_{2g} orbitals with only one unpaired 4d electron in the higher e_g orbitals, corresponding to the case of strong field with low spin (i.e. $t_{2g}^6 e_g$ configuration with S=1/2). This point is also suitably supported by the band structures and DOS for Fe and Ru doped systems in Figures 2c,d and 3c,d, respectively.

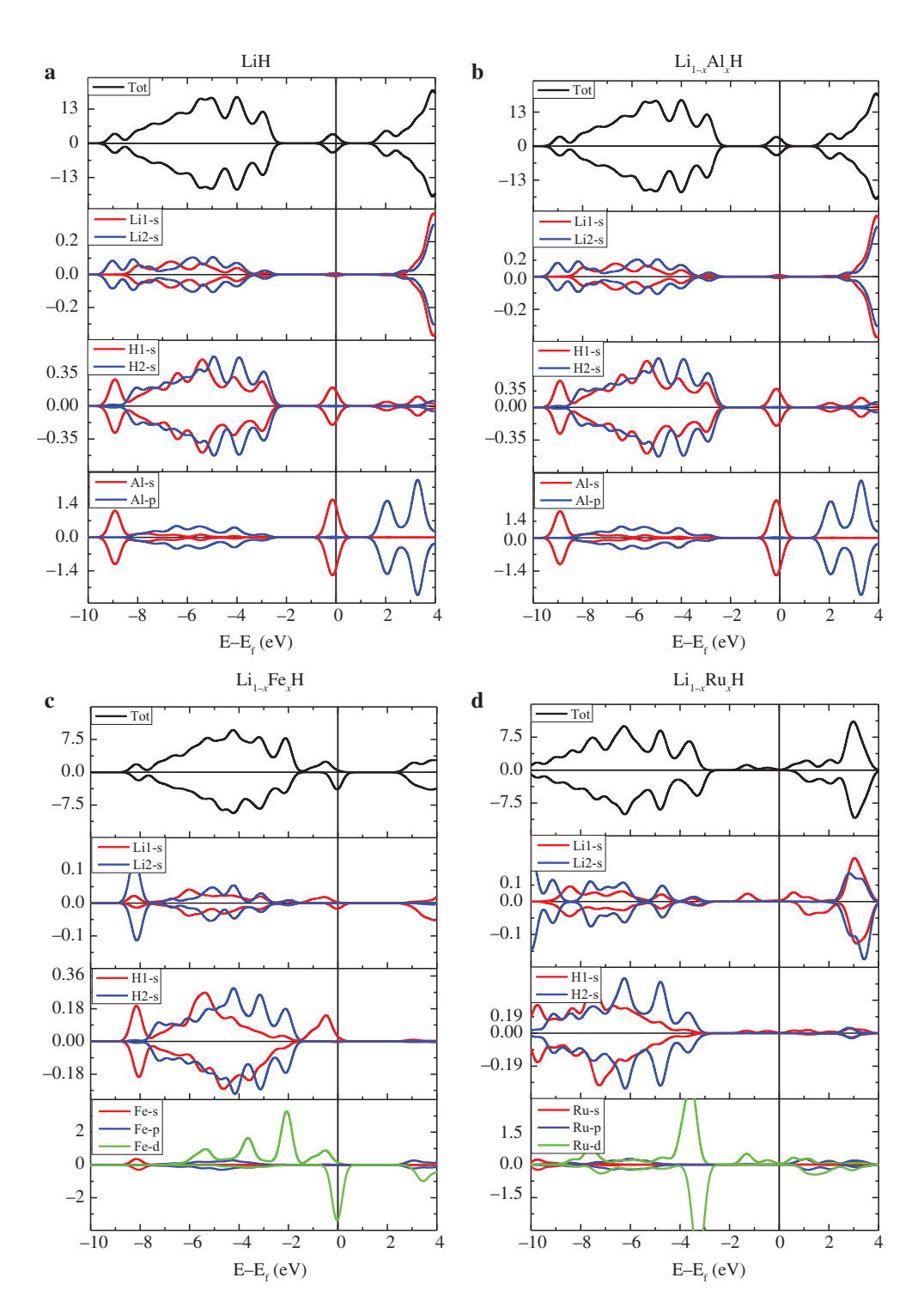
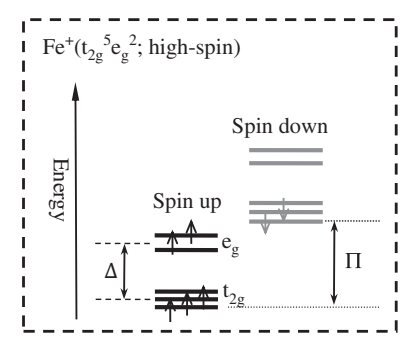


Figure 3: Total and projected DOS for the pure LiH and Li_xM_{1-x}H. H1 and Li1 denote the nn H and nnn Li, respectively. H2 and Li2 stand for the corresponding atoms far away from the dopants M. (a) LiH, (b) Li_{1-x}Al_xH (c) Li_{1-x}Fe_xH, and (d) Li_{1-x}Ru_xH.

3.4 Charge density

The charge distribution in both pure and doped LiH systems can be analyzed here. On the Pauling scale, H has a higher electronegativity of 2.20, while Li has a lower value of 0.98. Thus, in LiH, atomic H has a more potential to

attract electrons than atomic Li and induce ${\rm Li}^+$ cation and ${\rm H}^-$ anion. The 2D charge density plot of ${\rm Li}_{1-x}{\rm M}_x{\rm H}$ is shown in Figure 5, which clearly shows the charge density surface around H and TM (Fe and Ru) atoms. These charge density contours exhibit the ionic character of LiH and covalent nature of ${\rm Li}_{1-x}{\rm M}_x{\rm H}$, respectively.



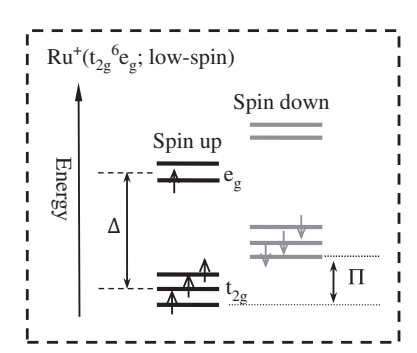


Figure 4: The electronic spin configuration of d^7 transition-metal ions $Fe^+(t_{2g}{}^5e_g{}^2;$ high-spin) and $Ru^+(t_{2g}{}^6e_g;$ low-spin) in an octahedral ligand field. Based on the crystal field theory, the high- or low-spin depends on a competition between the crystal field stabilization energy (Δ) and the intra-orbital electron pairing energy (Π).

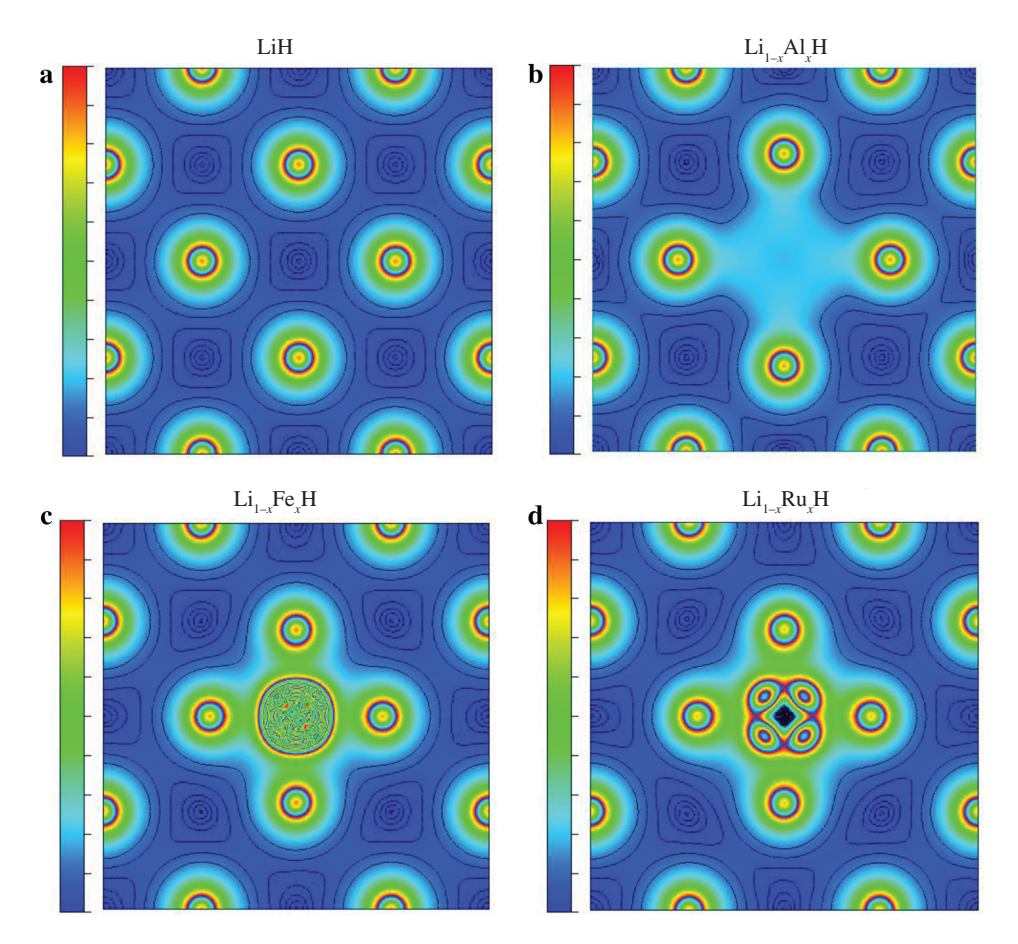


Figure 5: Electron density of $Li_{1-x}M_xH$. The central atoms of the plane are Li or M atom. The colors are corresponding to different densities: red-higher; blue-lower. (a) LiH, (b) $Li_{1-x}Al_xH$, (c) $Li_{1-x}Fe_xH$, and (d) $Li_{1-x}Ru_xH$.

The electronegativity values of Al, Fe, and Ru are 1.61, 1.83, and 2.20, respectively. Thus, H and M (=Al, Fe, and Ru) may show affinity for electrons. This point is also verified by the Mulliken charge of M in Table 3. Hydrides of Al are well-known covalent compounds [59, 60] in view of Al electronegativity larger and smaller than Li and H, respectively. Thus, the Al-H bond is expected to be more covalent than the host Li-H one from the lower difference

in electronegativity of the former, as pointed out for complex metal aluminum hydrides [5]. From the contours in Figure 5, Li continues to show absence of charge density after doping. The electron density is directed along the six principal M–H bonds, validating the presence of covalent bonding. Meanwhile, the overlap populations (OP) in Table 3 reaffirm the significant covalency of Fe–H and Ru–H bonds and mild covalency of Al–H bonds as well.

3.5 Optical Properties

The imaginary part $\varepsilon_{\text{Im}}(\omega)$ is calculated from the momentum matrix elements between the occupied and unoccupied wave functions within the selection rules. The real part $\varepsilon_{Re}(\omega)$ is obtained from the Kramers-Kronig relationship [61]. Then the other linear optical properties [i.e. electron energy loss spectrum $L(\omega)$, absorption coefficient $\alpha(\omega)$, reflectivity $R(\omega)$, refractive index $n(\omega)$, and extinction coefficient $k(\omega)$] can be further obtained [62]. The related results are presented in Figures 6 and 7 for the energy range up to 15 eV.

3.5.1 Optical Absorption

The absorption coefficients $\alpha(\omega)$ (=2 $k\omega/c$) are calculated and presented in Figure 6, in which the absorption spectra in the range of 0-4.5 eV are magnified and shown in the inset. The quantity k is the imaginary part of the refractive index. For pure LiH, the absorption coefficient increases obviously in the energy range of 4.1-10.2 eV, in the UV and far-UV region, with the strong absorption in the range of 9–11 eV. The absorption spectra of LiH show a number of well-defined extreme points, marked as A (\sim 6.6 eV), B (\sim 7.5 eV), C(\sim 10.2 eV), and D(\sim 11.4 eV), quantitatively in accordance with the experimental findings [63–65]. After M doping, these peaks (A, B, C, and D) exhibit red-shifts to the lower energy regions (labeled as A', B', C', and D', respectively), in the UV-Vis region. However, the intensity of the absorption spectra decreases, and the width becomes narrower. Especially, a new wide peak F' (\sim 0.6– 3.0 eV) appears in the visible and infrared regions for the-Ru doped system because of the d-d transition bands.

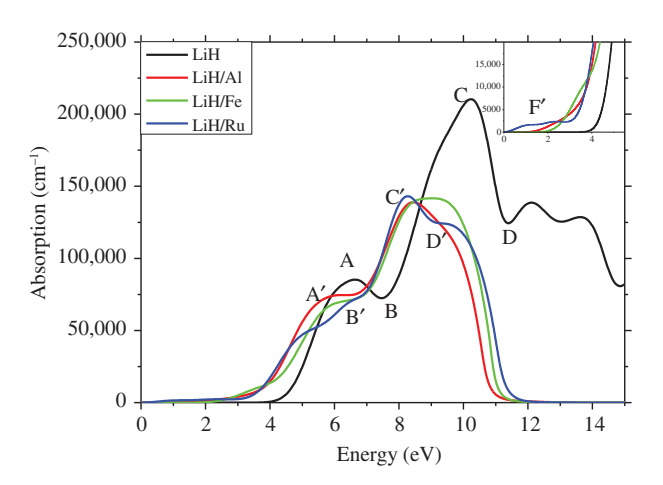


Figure 6: Absorption coefficient $\alpha(\omega)$ of LiH with and without the dopants. All absorption peaks show some red-shifts for the doped systems related to those for pure LiH.

So, TM doping may effectively improve the utilization of visible and infrared light.

3.5.2 Dielectric Function

The calculated complex dielectric functions $\varepsilon(\omega)$ = $\varepsilon_{\rm Re}(\omega) + i\varepsilon_{\rm Im}(\omega)$ of Li_xM_{1-x}H are presented in Figure 7a,b, which exhibit isotropy along various directions. The real part $\varepsilon_{Re}(\omega)$ describes the polarizability of the materials, whereas the imaginary part $\varepsilon_{\rm Im}(\omega)$ is related to the absorption $\alpha(\omega)$ of the systems. The static optical dielectric constants $\varepsilon(0)$ are 2.52, 2.21, 2.15, and 2.78 for LiH, Li_xAl_{1-x}H, $\text{Li}_{x}\text{Fe}_{1-x}\text{H}$, and $\text{Li}_{x}\text{Ru}_{1-x}\text{H}$, respectively. Interestingly, ε_{Re} of $\text{Li}_{x}\text{Ru}_{1-x}\text{H}$ at very low energy region (e.g. 10^{-4} –0.01 eV for the THz band) exhibits a moderate increase (by no less than 5 %) as compared with pure LiH. This may support the valid method to increase the dielectric constant of materials at THz region with TM dopants [66, 67]. Similarly, the curve of the calculated $\varepsilon_{Re}(\omega)$ has the extreme points at A (\sim 5.0 eV), B (\sim 7.0 eV), C (\sim 8.1 eV), and D (\sim 10.5 eV) for LiH, while the corresponding extreme points (A', B', C', and D') exhibit dissimilar red shifts for the doped systems. A new extreme point F' (\sim 1.3 eV) occurs for $Li_xRu_{1-x}H$, which is comparable with the peak F' in the absorption spectra. In the real dielectric function, there are some negative regions of 9.7-11.3, 8.2-10.6, 8.5-10.8, and 8.2–11.0 eV for LiH, $Li_xAl_{1-x}H$, $Li_xFe_{1-x}H$, and $Li_x Ru_{1-x}H$, respectively. The incident light in these regions cannot propagate because of the imaginary wave vector K in the equation of wave motion $K^2c^2 = \omega^2 \varepsilon$, reflecting the metallic nature of the materials at these frequencies.

From Figure 7a,b, the extreme points (A \sim 5.9 eV, B \sim 7.4 eV, C \sim 9.1 eV, and D \sim 11.1 eV) of $\varepsilon_{\rm Im}(\omega)$ are close to those of $\varepsilon_{\rm Re}(\omega)$ for LiH. Similarly, the corresponding extreme points (A', B', C', and D') also red-shift to some degrees for the doped systems, and a new extreme point F' (\sim 0.8 eV) occurs in the visible region of $\varepsilon_{\rm Im}(\omega)$ for $Li_xRu_{1-x}H$. So, the doped systems may effectively improve the utilization of visible light and infrared light. The curve $\varepsilon_{\rm Im}(\omega)$ falls to 0 at below 4.0 eV for LiH, which is comparable with the direct bandgap at X point. The peaks of the imaginary part $\varepsilon_{\rm Im}(\omega)$ are corresponding to the different inter-band transitions.

3.5.3 Optical Conductivity

The frequency-dependent conductivity $\sigma(\omega)$ has both real and imaginary parts: $\sigma = \sigma_{\rm Re} + {\rm i}\sigma_{\rm Im}$, which can be expressed in terms of the dielectric functions as $\sigma_{Re} =$ $\frac{\omega}{4\pi} \epsilon_{Im}$, $\sigma_{Im} = i \frac{\omega}{4\pi} (1 - \epsilon_{Re})$. To make sure that the dc

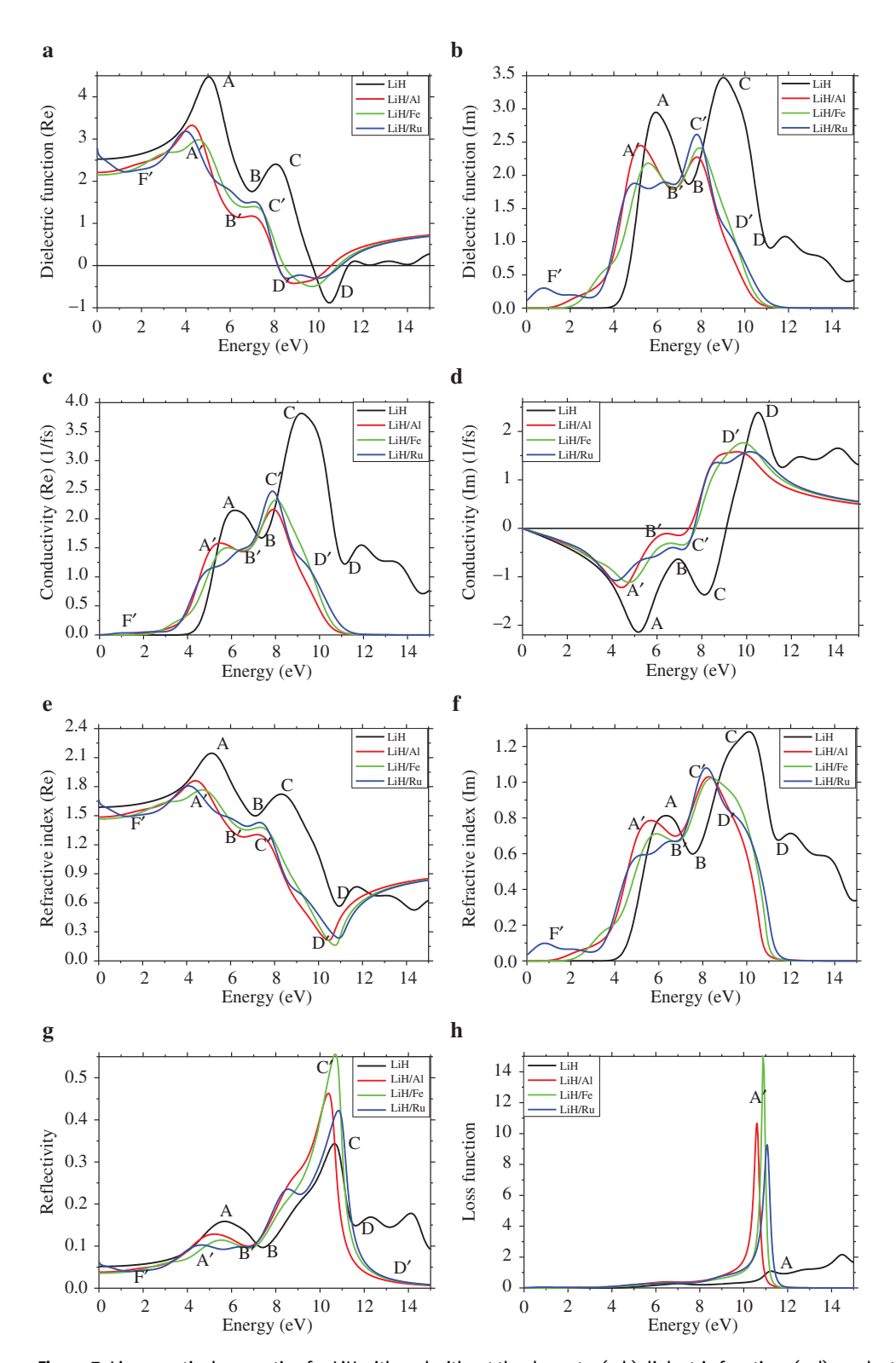


Figure 7: Linear optical properties for LiH with and without the dopants. (a,b) dielectric function, (c,d) conductivity, (e,f) refractive index, (g) reflectivity, (h) loss function.

conductivity $\sigma_{dc} = \sigma_{Re}(0) = 0$, we set the Drude damping parameter as 10^{-4} eV [65, 68]. The optical conductivity (OC) spectra are shown in Figure 7c,d. It can be found that

the real part of OC spectra reveals the similar shapes and the slight red shifts of the peak positions related to the absorption spectra. After doping, a new peak exists in the visible region, and the corresponding extreme points (A', B', C', and D') for doped systems also show some red shifts related to those (A. B. C. and D) for pure LiH.

3.5.4 Refractive Index and Extinction Coefficient

The complex dielectric constant is an elementary parameter involving many important properties of materials. From the relationships between refractive index N = n + 1 $ik = \sqrt{\varepsilon}$ and dielectric constant $\varepsilon_{Re} = n^2 - k^2$, $\varepsilon_{Im} = 2nk$, the real and imaginary parts of the complex refractive index can be given as

$$n(\omega) = \sqrt{\frac{1}{2} \left(\sqrt{\varepsilon_{Re}^2 + \varepsilon_{Im}^2} + \varepsilon_{Re} \right)}$$

$$k(\omega) = \sqrt{\frac{1}{2} \left(\sqrt{\varepsilon_{Re}^2 + \varepsilon_{Im}^2} - \varepsilon_{Re} \right)}.$$
 (2)

The refraction index $n(\omega)$ and extinction coefficient $k(\omega)$ vs. photon energy for $\text{Li}_{x}\text{M}_{1-x}\text{H}$ are shown in Figure 7e,f. Comparing Figure 7a with Figure 7e, one can conclude that the curves of refraction index $n(\omega)$ are analogous to $\varepsilon_{Re}(\omega)$. The refraction indexes for zero frequency are obtained as 1.59, 1.49, 1.61, and 1.67 for LiH, Li_xAl_{1-x}H, Li_xFe_{1-x}H, and Li_xRu_{1-x}H, respectively. The original extreme points A (\sim 5.1 eV), B (\sim 7.1 eV), C (\sim 8.3 eV), and D (\sim 10.9 eV) show different red shifts in the doped systems. Remarkably, a new extreme point F' appears at \sim 1.98 eV for $\text{Li}_x \text{Ru}_{1-x} \text{H}$, which is comparable with the peak position F' in the absorption spectra. The profiles of the extinction coefficient $k(\omega) = \varepsilon_{\rm Im}/(2n)$ in Figure 7f are similar to $\varepsilon_{\rm Im}$ in Figure 7b. The photon energies for the peaks A, B, C, and D are 6.3, 7.5, 10.1, and 11.4 eV, respectively. The slight differences between $k(\omega)$ and ε_{Im} may rise from the adopted calculation method, which is not well justified for the materials with some absorption coefficients [69].

3.5.5 Optical Reflectivity Coefficient

Optical reflectivity is calculated from the refractive index by using $R(\omega) = |(1 - N)/(1 + N)|^2 = [(n - 1)^2 + k^2]/(n + N)$ $[(n+1)^2 + k^2]$ and presented in Figure 7g. With respect to the optical reflectivity coefficient 5.2 % at 0 eV for pure LiH, doping with metal M induces some decreases by 1.4 % and 1.7 % for M=Al and Fe and an increase by 1.0 % for M=Ru, respectively. The optical reflectivity coefficient of $Li_xM_{1-x}H$ is largely lower than pure LiH in the infrared, visible, and near UV regions (<7.2 eV) and higher in the far UV region (7.2–11.5 eV).

3.5.6 Energy Loss Function

Involving with important information related to the energy loss of fast moving electrons in materials, the electron energy loss function is calculated from $L(\omega) = \text{Im}(-1/\varepsilon(\omega))$ and displayed in Figure 7h. The energy loss of LiH is almost zero below 4.2 eV and very low in the entire UV-Vis region. However, the curves of loss function for the doped systems are changed dramatically in the region from 10 to 12 eV. A number of broad and small peaks termed "plasmons" arise in the loss function for pure LiH, whereas a sharper and narrower peak referred to "longitudinal exciton" occurs for the M-doped LiH crystals. The resonance peak for the doped LiH systems locates in the region of 10.6–11.1 eV, corresponding to the steep drop of the reflection coefficient $R(\omega)$ after 10.3 eV.

3.6 Thermodynamic Properties and **Hydrogen Storage**

The reactions related to the formation of LiH and $\text{Li}_x M_{1-x} H$ are as follows:

$$Li + \frac{1}{2}H_2 \rightarrow LiH$$

$$x Li + (1 - x) M + \frac{1}{2}H_2 \rightarrow Li_x M_{1-x}H$$
 (3)

To calculate the formation heat of these reactions, the total energies of element Li, metal-atom M, and hydrogen molecule are subtracted from the hydrides LiH and $\text{Li}_{x}\text{M}_{1-x}\text{H} \text{ with } x = 1 \text{ and } x = 0.96875$:

$$\Delta H(\text{LiH}) = E_{\text{tot}}(\text{LiH}) - E_{\text{tot}}(\text{Li}) - \frac{1}{2}E_{\text{tot}}(\text{H}_2)$$

$$\Delta H(\text{Li}_x \text{M}_{1-x} \text{H}) = E_{\text{tot}}(\text{Li}_x \text{M}_{1-x} \text{H}) - xE_{\text{tot}}(\text{Li})$$

$$- (1-x)E_{\text{tot}}(\text{M}) - \frac{1}{2}E_{\text{tot}}(\text{H}_2)$$
 (4)

The total energies obtained with the optimized structures of LiH, Li, and Ru are used for the studied systems. The total energy of hydrogen molecule is $E_{\text{tot}}(\text{H}_2) \approx -2.332 \text{ Ry}$, adjacent to -2.330 Ry in [70] and -2.320 Ry in [7]. The computed formation enthalpy is listed in Table 3. The formation heat -94.06 kJ/molH of LiH is actually close to the experimental values $(\approx -90.5 \text{ kJ/mol H} [47] \text{ and } -116.3 \text{ kJ/mol H} [71]) \text{ and }$ the previous theoretical results (≈-89 kJ/mol H [7], -87 kJ/mol H [72], -81 kJ/mol H [73], and -85 kJ/mol

H [6]) obtained with different methods. The slight discrepancies can be ascribed to the different calculation methods. Importantly, the addition of metal M to LiH reduces the stability of LiH and may consequently improve the dehydrogenation process. The order (Al < Fe < Ru) of the magnitude of ΔH can be illustrated by the stronger crystal fields of the d^7 clusters, especially the low spin $(S = 1/2) \operatorname{Ru}^+[t_{2g}{}^6 e_g]$ group as compared with the high spin (S = 3/2) Fe⁺ [$t_{2g}^5 e_g^2$] one [58]. Therefore, the destabilization effect is enhanced with metal dopants without obviously sacrificing the storage capacities.

The thermodynamic properties of the hydrides can be described with the standard Gibbs free energy $\Delta G = \Delta H - T\Delta S$. For the standard zero Gibbs free energy at the decomposition temperature and a constant pressure [18], the temperature can be estimated from enthalpy and entropy changes by using $\Delta H = T\Delta S$. As the entropy changes of a solid are much smaller than that of the corresponding gas during heating, the entropy change in the decomposition reaction is dominated by the entropy loss of the gaseous hydrogen. For most metal hydrides, the entropy change (corresponding to a mole of gas transforming into the solid) is $\Delta S \approx 130.7 \text{ J/mol K} [74?]$ at the standard pressure and temperature. From the thermodynamic relation $T_{\rm dec} = \Delta H/\Delta S$, the temperature of dehydrogenation can be estimated from the calculated $\Delta H(H_2)$. This yields the significantly overestimated decomposition temperature of 1439 K for pure LiH, as compared with the experimental value 993 K [71]. The calculated $T_{\rm dec}$ may display a slight or significant decrease with dopants, as mentioned for similar doped hydrides [8]. From [21], the entropy change is estimated in the range of 95-140 J/mol K for most dehydrogenation reactions. Adoption of the upper limit of 140 J/mol K and the above enthalpy change yields $T_{\rm dec} \approx 1343$ K, which is still higher than but closer to the measured 993 K [71].

The destabilization of LiH with M dopants so as to reduce the dehydriding temperature may be an important method for practical applications. From Table 3, ΔH decreases from pure LiH to doped systems and shows the order Ru > Fe > Al, corresponding to the dehydriding temperatures of 606, 570, and 522 K for Ru-, Fe-, and Al-doped systems, respectively, with the upper limit of entropy change. So, the Al-substituted system is possibly the most suitable candidate for hydrogen storage due to the high hydrogen content and low dehydriding temperature, which is consistent with the various studies on the complex alkali metal hydrides [1?]. It is noted that increasing concentration of M dopants would induce new complex metal hydrides and hence further decreases of ΔH , as mentioned in [5].

4 Conclusions

In order to improve the hydrogen storage properties of the Li-based hydrides, such as $Li_{1-x}M_xH$ (M=Al, Fe, and Ru), the DFT studies are carried out for LiH without and with M dopants. The results of formation heats for LiH with and without M as well as their electronic structures confirm that doping metals M may depress the stability of the systems and favorably improve the dehydrogenating properties of LiH. The dopants indeed enhance the visible light absorption of LiH by inducing some new d-d transition bands in the visible region. The calculated formation heats reveal that the Al-substituted systems can yield the greatest reduction of the dehydriding temperature with respect to pure LiH. Present calculations suggest that Al could be a better substituent than Fe and Ru for enhancing the hydrogen storage properties of LiH. As is known, adding metal dopants to LiH may improve the hydrogen diffusion and reduce the absorption/desorption time. The kinetic properties will be studied in detail with kinetic Monte Carlo method in the future work.

Acknowledgments: This work was financially supported by the National Natural Science Foundation of China grant no. 11764028 and the Sichuan Province Academic and Technical Leaders Support Fund [Y02028023601041]. Great thanks are also given to Prof. Kai-Lai Xu of the Key Laboratory of Green Chemistry and Technology of Ministry of Education, Sichuan University for her help in MS 8.0 calculations.

References

- [1] B. Sakintuna, F. Lamari-Darkrim, and M. Hirscher, Int. J. Hydrogen Energy 32, 1121 (2007).
- [2] M. Bououdina, D. Grant, and G. Walker, Int. J. Hydrogen Energy 31, 177 (2006).
- [3] W. Mueller, J. Blackledge, and G. Libowitz, Metal Hydrides, Academic Press, New York 1968.
- [4] Y. Fukai, The Metal-Hydrogen System: Basic Bulk Properties, Springer Science & Business Media 2006.
- [5] T. Kelkar, S. Pal, and D. G. Kanhere, ChemPhysChem 9, 928 (2008).
- [6] R. Napán and E. L. Peltzer y Blancá, Int. J. Hydrogen Energ. 37, 5784 (2012).
- [7] Y. Bouhadda, A. Rabehi, and S. Bezzari-Tahar-Chaouche, Revue des Energies Renouvelables 10, 545 (2007).
- M. Lakhal, M. Bhihi, A. Benyoussef, A. El Kenz, M. Loulidi, et al., Int. J. Hydrogen Energy 40, 6137 (2015).
- [9] Z. Xiong, C. K. Yong, G. Wu, P. Chen, W. Shaw, et al., Nat. Mater. 7, 138 (2007).
- [10] P. Gislon and P. P. Prosini, Int. J. Hydrogen Energy 36, 240 (2011).

- [11] E. Dologlou, J. Appl. Phys. 107, 083507 (2010).
- [12] M. M. Sigalas, J. Nanosci. Adv. Tech. 1, 12 (2015).
- [13] S. Banger, V. Nayak, and U. P. Verma, J. Phys. Chem. Solids **115**, 6 (2018).
- [14] D. Mukherjee, B. D. Sahoo, K. D. Joshi, S. C. Gupta, and S. K. Sikka, J. Appl. Phys. 109, 103515 (2011).
- [15] G. Barkhordarian, T. Klassen, and R. Bormann, J. Phys. Chem. B 110, 11020 (2006).
- [16] M. Y. Song, S. N. Kwon, H. R. Park, and S.-H. Hong, Int. J. Hydrogen Energy 36, 13587 (2011).
- [17] M. Cabo, S. Garroni, E. Pellicer, C. Milanese, A. Girella, et al., Int. J. Hydrogen Energy 36, 5400 (2011).
- [18] M. Bhihi, M. Lakhal, H. Labrim, A. Benyoussef, A. E. Kenz, et al., Chin. Phys. B 21, 097501 (2012).
- [19] J. J. Reilly and R. H. Wiswall, Inorg. Chem. 6, 2220 (1967).
- [20] J. J. Reilly and R. H. Wiswall, Inorg. Chem. 7, 2254 (1968).
- [21] S. V. Alapati, J. K. Johnson, and D. S. Sholl, J. Phys. Chem. B 110, 8769 (2006).
- [22] I. P. Jain, P. Jain, and A. Jain, J. Alloys Compd. 503, 303 (2010).
- [23] S. N. Nyamsi, V. Yartys, and M. Lototskyy, 1st Africa Energy Materials Conference, 28-31 March 2017 5 (4, Part 2), 10533 (2017).
- [24] X. Chen, J. Zou, X. Zeng, and W. Ding, J. Alloys Compd 701, 208 (2017).
- [25] Z. Xin, J. Zhang, K. Sordakis, M. Beller, C.-X. Du, et al., ChemSusChem 11, 2077 (2018).
- [26] F. Moser and F. Urbach, Phys. Rev. 102, 1519 (1956).
- [27] G. I. Pilipenko, Phys. Solid State 47, 1573 (2005).
- [28] J. Bruns, D. van Gerven, T. Klüner, and M. S. Wickleder, Angew. Chem. Int. Ed. 55, 8121 (2016).
- [29] CP2K devolop group, CP2K package (http://www.cp2k.org,
- [30] S. J. Clark, M. D. Segall, C. J. Pickard, P. J. Hasnip, M. J. Probert, et al., Z. Kristallogr. 220, 567 (2005).
- [31] R. Jaradat, M. Abu-Jafar, I. Abdelraziq, R. Khenata, D. Varshney, et al., Phase Transit. 90, 914 (2017).
- [32] A. B. Kunz and D. J. Mickish, J. Phys. C: Solid State Phys. 6, L83
- [33] A. B. Kunz and D. J. Mickish, Phys. Rev. B 11, 1700 (1975).
- [34] M. J. van Setten, V. A. Popa, G. A. de Wijs, and G. Brocks, Phys. Rev. B 75, 035204 (2007).
- [35] J. VandeVondele, M. Krack, F. Mohamed, M. Parrinello, T. Chassaing, et al., Comput. Phys. Commun. 167, 103 (2005).
- [36] M. Iannuzzi, T. Chassaing, T. Wallman, and J. Hutter, CHIMIA Int. J.Chem. 59, 499 (2005).
- [37] G. Lippert, J. Hutter, and M. Parrinello, Theor. Chem. Acc. 103, 124 (1999).
- [38] J. P. Perdew, K. Burke, and M. Ernzerhof, Phys. Rev. Lett. 77, 3865 (1996).
- [39] J. VandeVondele and J. Hutter, J. Chem. Phys. 127, 114105 (2007).
- [40] S. Goedecker, M. Teter, and J. Hutter, Phys. Rev. B 54, 1703 (1996).
- [41] C. Adamo and V. Barone, J. Chem. Phys. 110, 6158 (1999).
- [42] A. M. Rappe, K. M. Rabe, E. Kaxiras, and J. D. Joannopoulos, Phys. Rev. B 41, 1227 (1990).
- [43] L. N. Wu, S. Y. Wu, L. J. Zhang, X. S. Liu, and G. J. Zhang, Z. Naturforsch. A 74, 59 (2019).

- [44] A. Manzar, G. Murtaza, R. Khenata, S. Muhammad, and Hayatullah, Chin. Phys. Lett. 30, 047401 (2013).
- [45] C. Kittel, Introduction to Solid State Physics. John Wiley & Sons Inc, New York 1986.
- [46] F. D. Murnaghan, Proc. Natl. Acad. Sci. U.S.A. 30, 244 (1944).
- [47] R. C. Weast, CRC Handbook of Chemistry and Physics, CRC Press Inc., Boca Raton, Florida 1982.
- [48] D. R. Stephens and E. M. Lilley, J. Appl. Phys. 39, 177 (1968).
- [49] A. G. Ryabukhin, V. E. Roshin, A. V. Roshin, Russ. Metall. (Metally) 2007, 98 (2007).
- [50] S.-Y. Wu, X.-Y. Gao, J.-Z. Lin, and Q. Fu, J. Alloy. Compd. 424, 55
- [51] L. N. Wu, S. Y. Wu, X. S. Liu, S. Y. Zhong, and F. Zhang, Phys. Status Solidi B 255, 1800026 (2018).
- [52] L. N. Wu, S. Y. Wu, S. Y. Zhong, L. J. Zhang, and Q. Q. Tan, Magn. Res. Chem. 56, 196 (2018).
- [53] T. Seddik, R. Khenata, O. Merabiha, A. Bouhemadou, S. Bin-Omran, et al., Appl. Phys. A 106, 645 (2012).
- [54] J. P. Perdew, W. Yang, K. Burke, Z. Yang, E. K. U. Gross, et al., Proc. Natl. Acad. Sci. 114, 2801 (2017).
- [55] G. I. Pilipenko, A. A. Sabirzyanov, D. V. Oparin, V. G. Stepanov, and F. F. Gavrilov, J. Phys. Condens. Matter 4, 4055 (1992).
- [56] J.-L. Bredas, Mater. Horiz. 1, 17 (2014).
- [57] F. A. Cotton, Chemical Applications of Group Theory, John Wiley & Sons, 2003.
- [58] A. S. Chakravarty, Introduction to the Magnetic Properties of Solids, Wiley, New York, 1980.
- [59] A. Peles, J. A. Alford, Z. Ma, L. Yang, and M. Y. Chou, Phys. Rev. B 70, 165105 (2004).
- [60] P. Vajeeston, P. Ravindran, A. Kjekshus, and H. Fjellvag, Phys. Rev. B 69, 020104 (2004).
- [61] M. Gaidorfmmodeš, K. Hummer, G. Kresse, J. Furthmüller, and F. Bechstedt, Phys. Rev. B 73, 045112 (2006).
- [62] J. Sun, H. T. Wang, J. L. He, and Y. J. Tian, Phys. Rev. B 71, 125132 (2005).
- [63] W. B. Zimmerman and D. J. Montgomery, Phys. Rev. 120, 405 (1960).
- [64] B. L. Dvinyaninov, F. F. Gavrilov, and G. I. Smetanin, J. Appl. Spectros. 6, 38 (1967).
- [65] F. E. Pretzel and C. C. Rushing, J. Phys. Chem. Solids 17, 232 (1961).
- [66] A. J. L. Adam, J. Infrared Millim. Te. 32, 976 (2011).
- [67] S. Tangwancharoen, P. Thongbai, T. Yamwong, and S. Maensiri, Mater. Chem. Phys. 115, 585 (2009).
- [68] I. R. Hooper and J. R. Sambles, Phys. Rev. B 65, 165432 (2002).
- [69] A. A. Lavrentyev, B. V. Gabrelian, V. T. Vu, L. N. Ananchenko, L. I. Isaenko, et al., Opt. Mater. 66, 149 (2017).
- [70] M. Lakhal, M. Bhihi, H. Labrim, A. Benyoussef, S. Naji, et al., Int. J. Hydrogen Energy 38, 8350 (2013).
- [71] W. Grochala and P. P. Edwards, Chem. Rev, 104, 1283 (2004).
- [72] C. Wolverton, V. Ozolins, and M. Asta, Phys. Rev. B 69, 144109 (2004).
- [73] K. Miwa, N. Ohba, S. Towata, Y. Nakamori, and S. Orimo, Phys. Rev. B 69, 245120 (2004).
- [74] H. H. Van Mal, K. H. J. Buschow, and A. R. Miedema, J. Less Common Met. 35, 65 (1974).